Progress In Electromagnetics Research C, Vol. 169, 138–148, 2026

PIER C

(Received 17 March 2026, Accepted 10 April 2026, Scheduled 26 April 2026)

Design of a Three-Layer SIW Broadband 1×4 Dipole Patch Array Antenna Driven by Slot Feeding

Mingming Gao, Ruize Huang*, Xuan Du, and Bowen Tao

School of Electronics and Information Engineering, Liaoning Technical University, Huludao 125105, China

ABSTRACT: To address the demand for broadband, high-gain antennas in millimeter-wave communications, this paper proposes a stacked dipole patch array antenna based on substrate-integrated waveguide (SIW) technology. The design employs a three-layer structure with slot-coupled feeding to enhance radiation performance. First, an SIW feeding structure is integrated into the bottom layer to ensure efficient signal coupling. Second, the middle layer features an innovatively designed "wrench-shaped" patch with metal vias, which not only effectively broadens the bandwidth but also enhances gain in conjunction with the rectangular patches on both sides. Finally, rectangular dipole patches are introduced in the top layer as parasitic elements to further optimize high-frequency performance. Through a 1-to-4 corporate-feed power divider network, the antenna achieves a measured impedance bandwidth of 24.42% (24.12 GHz–30.83 GHz) and a center frequency gain of 11.02 dBi. While achieving miniaturization, this antenna combines high bandwidth with high gain, demonstrating its application potential in next-generation millimeter-wave wireless communication.

1. INTRODUCTION

SIWs are currently the most mature and widely used structures among substrate-integrated circuits (SICs) and have been discussed in numerous studies [1, 2]. Modern wireless communication systems demand low-cost, high-integration, and multifunctional capabilities [3]. As a novel type of microwave transmission line, SIWs utilize metal vias on a dielectric substrate coated with metal on both sides to achieve waveguide propagation, combining the advantages of traditional waveguides and microstrip transmission lines. They can be used in the design of high-performance millimeter-wave circuits and antennas [4–8].

Traditional microstrip antennas generally exhibit low gain and narrow bandwidth. To improve the gain performance of microstrip antennas, researchers have proposed methods such as using dielectric plates with low permittivity, adding parasitic patches, and configuring antenna arrays. With the emergence of electromagnetic metamaterials at the beginning of this century, researchers have utilized metamaterials to modify antenna substrates, antenna coatings, and radiation structures, thereby suppressing surface waves on the antenna to enhance antenna gain [9]. Typically, an SIW is employed as a feeding method in combination with microstrip antenna arrays to achieve high efficiency and high gain [10–12]. However, due to the quasi-closed structure and high-Q characteristics of substrate-integrated waveguides, the resulting antennas exhibit narrow bandwidths [13, 14]. To expand the antenna's impedance bandwidth, researchers have conducted extensive studies and found that introducing a multilayer structure with coupled feeding [15–17] can effectively broaden the impedance bandwidth. The principle lies in using a substrate-integrated waveguide as the feeding structure, which is connected to the upper-layer structure via a specific coupled feeding method, thereby integrating the microstrip patch with the substrate-integrated waveguide structure.

In recent years, researchers have conducted extensive work to achieve broadband, miniaturized, and highly integrated antenna designs. Ref. [18] employs half-mode SIW (HMSIW) technology to design a compact, low-profile 4-port multiple-input multiple-output (MIMO) antenna. By incorporating a rectangular slot in the center of the open wall, the antenna excites both the odd and even TE_{110} modes to a similar degree, providing an impedance bandwidth of –10 dB from 5.63 to 5.87 GHz. Ref. [19] presents a substrate-integrated cavity (SIC) circularly polarized array antenna for the Ku-band. By introducing a pair of crescent-shaped parasitic patches along the diagonal of the SIC aperture and a bottom-fed longitudinal slot, the amplitudes of the TM_{211} and TM_{121} resonance modes are equalized with a 90° phase difference. Combined with a 2×2 element sequentially rotating feed network, the antenna achieves a measured effective bandwidth of 10.74–13.30 GHz (21.3%) and a maximum gain of 14.5 dBi within the passband. Ref. [20] describes a multilayer microstrip patch array antenna utilizing a three-layer substrate integrated waveguide (SIW) feeding network laminated onto a four-layer dielectric substrate. This design operates across the 11.2–13.6 GHz band with a relative bandwidth of 19.35% and a peak gain of 17.1 dBi, demonstrating the advantages of low loss and high efficiency. In [21], a broadband circularly polarized magneto-dipole antenna array with SIW feeding is reported. The antenna elements are coupled to the SIW cavity via cross-shaped rectangular slits to excite a pair of chamfered magneto-dipoles; additionally, an L-shaped parasitic patch is introduced to extend

---

* Corresponding author: Ruize Huang (2844484378@qq.com).

doi:10.2528/PIERC26031706

Published by THE ELECTROMAGNETIC ACADEMY

the circular polarization bandwidth. The measured impedance bandwidth of the 2×2 array is 21.8% (29.28–35.83 GHz), with an axial ratio bandwidth of 14% (31.29–35.83 GHz) and a peak gain of 14.1 dBic. Finally, Ref. [22] proposes an 8×8 double-layer antenna array based on SIW feeding, employing aperture coupling for interlayer interconnection. The bandwidth is enhanced by increasing the air cavity height. Experimental results indicate that the array achieves an impedance bandwidth of 16.3% (35.4–41.7 GHz), with a peak gain of 26.7 dBi and a radiation efficiency of 83.2%.

Based on the above theoretical and structural analysis, this paper proposes an antenna array with a three-layer dielectric structure. The bottom-layer feeding network uses a substrate-integrated waveguide structure and employs a slot-coupled feeding method to achieve a transition to the upper dielectric layer. The middle dielectric layer incorporates a wrench-shaped microstrip patch to increase bandwidth, with two rectangular patches placed on the upper and lower sides. Each patch is equipped with a metal via to enhance gain stability. The top layer employs a rectangular magneto-dipole patch as a parasitic patch. As an antenna element with broadband characteristics, the magneto-dipole antenna [23], after optimization and adjustment, integrates with the overall antenna structure to effectively expand the antenna bandwidth. The feeding network is designed based on a substrate-integrated waveguide (SIW) to accommodate a 1-to-4 corporate power divider, while the transition feeding structure employs a modified ground coplanar waveguide (GCPW)-SIW conversion structure. Simulation and measured results of the final antenna design show that it covers the frequency range of 24.12 GHz to 30.83 GHz, with a relative bandwidth of 24.42% and a maximum gain of 11.02 dBi. The antenna designed based on this structure achieves the objectives of broadband operation and stable directivity. Its frequency range of 24.12 GHz to 30.83 GHz covers China's 5G millimeter-wave frequency bands, the preliminary 5G frequency bands in Europe (24.25 GHz–27.5 GHz), and the authorized spectrum in the United States (27.5 GHz–28.35 GHz), thereby meeting the "global connectivity" requirements as a high-gain, broadband millimeter-wave antenna.

2. ANTENNA DESIGN

2.1. Array Element Design

The antenna element designed in this paper employs a stacked architecture consisting of three dielectric substrate layers and three metal layers, as illustrated in Fig. 1. All metal layers are fabricated using a copper-cladding process. The dielectric substrate is Rogers 5880, with a thickness of 1.016 mm, a relative permittivity of $\varepsilon_r = 2.2$, and a loss tangent of $\tan\delta = 0.0009$. From bottom to top, the structure is divided into a feeding layer, a coupling layer, and a radiation layer, which collectively form a complete "feed-coupling-radiation" electromagnetic energy transmission chain.

(1) The bottom layer utilizes a substrate integrated waveguide (SIW) structure as the feeding network. An equivalent waveguide cavity is formed by introducing periodic metallized vias into the dielectric substrate, with its effective width determined 1 and 2. To ensure effective confinement of electromagnetic energy within the cavity, the diameter of the metallized vias d_p and the pitch p must satisfy the design criteria: $d_p \geq 0.2p$ 3), and $d_p \leq 0.2W_{\mathit{eff}}$ 4), where W_{eff} represents the effective width of the SIW; L_{eff} is the equivalent length of the SIW cavity; f_r is the resonant frequency of the SIW resonator; c is the speed of light in a vacuum; m and n are the mode numbers; and L_c and W_c are the physical length and width of the resonator, respectively. Accordingly, $d_p = 0.4$ mm and $p = 0.8$ mm are selected. To achieve longitudinal energy transition from the SIW to the upper layers, a rectangular coupling slot is etched on the top metal surface of the cavity, leveraging the aperture coupling mechanism to efficiently transfer electromagnetic energy to the intermediate layer.

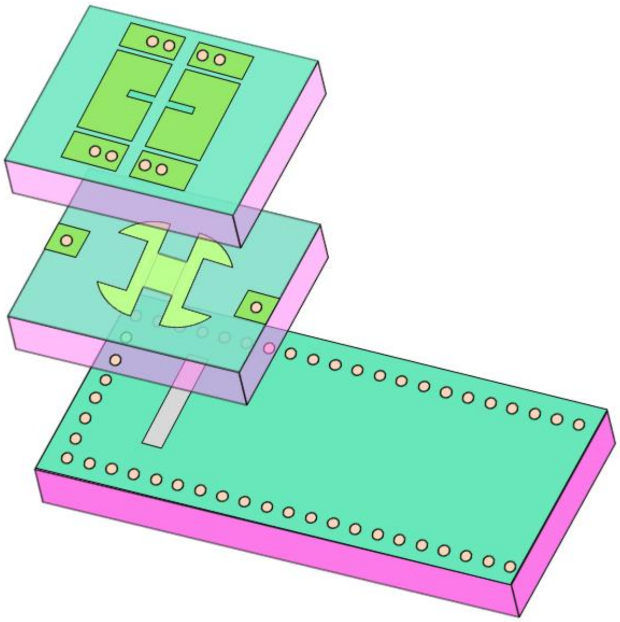

FIGURE 1. Array antenna structure diagram.

$$f_r = \frac{c}{2\sqrt{\epsilon_{\mathrm{r}}}}\sqrt{\frac{m}{L_{\mathit{eff}}^2} + \frac{n}{W_{\mathit{eff}}^2}} \tag{1}$$

$$L_{\mathit{eff}}\,(\text{or } W_{\mathit{eff}}) = \frac{L_c \text{ or } (W_c) \times d^2}{0.95 \times d_p} \tag{2}$$

$$\frac{\mathrm{d}p}{\mathrm{d}} < 2 \tag{3}$$

$$\frac{\mathrm{d}}{\mathrm{W}siw} < 2 \tag{4}$$

(2) Intermediate Coupling Layer: An innovative "wrench-shaped" microstrip patch is designed at the center of the upper surface of the intermediate dielectric layer. Through near-field coupling with the bottom-layer slot, this patch precisely captures the electromagnetic energy radiated from the SIW cavity and converts it into a quasi-TEM mode to feed the top-layer radiation structure. This specially shaped patch, together with the feeding slot, forms a dual-resonant circuit, effectively expanding the operating bandwidth by introducing an additional

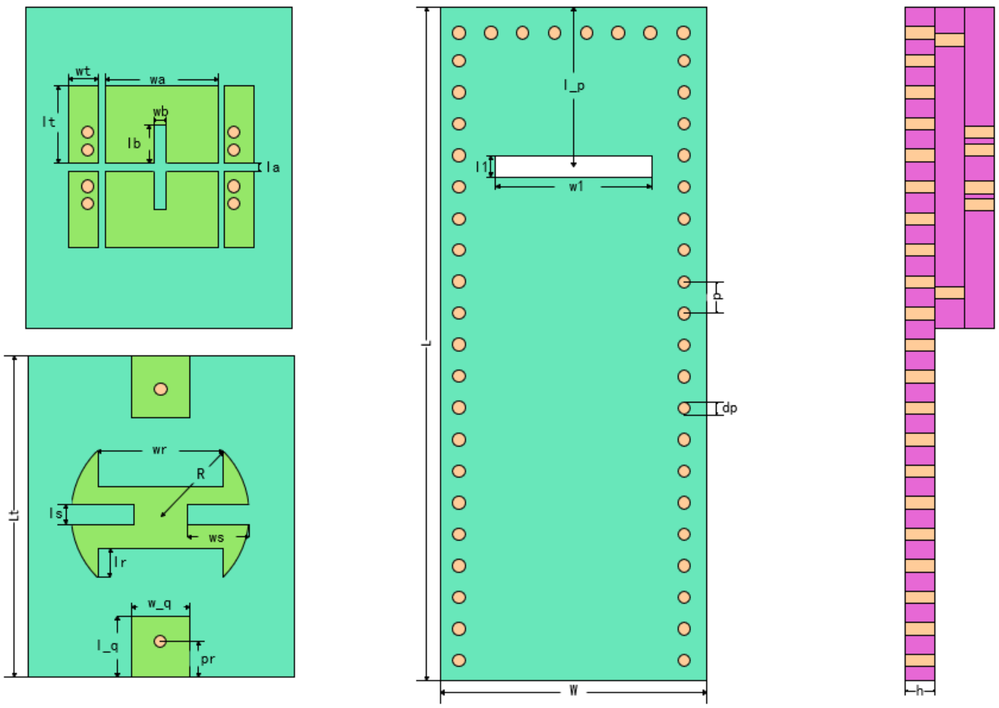

FIGURE 2. Array antenna planar diagram.

TABLE 1. Array antenna parameter dimensions.

parameter	size /mm	parameter	size /mm	parameter	size /mm
L	16.9	l_p	4.85	lr	1.27
W	7	Lt	10	ws	1.4
h	1.016	l_q	2	ls	0.6
dp	0.4	w_q	2	wa	2.7
p	0.8	pr	1.04	la	0.2
l1	0.5	R	2	wt	1
w1	3.3	wr	3	lt	2
wb	0.2	lb	1	–	–

resonance point. To further enhance energy transfer efficiency and gain flatness, two rectangular patches are symmetrically loaded on both sides of the wrench-shaped patch. These patches facilitate near-field energy exchange with the top-layer structure via magnetic coupling; simultaneously, they form a low-impedance path by connecting to the bottom reference ground through metallized vias, thereby suppressing energy leakage. Furthermore, this topology restricts the distribution of stray currents through boundary conditions, suppresses higher-order modes, and improves radiation purity.

(3) Top radiation layer: The top radiation structure consists of six rectangular patches acting as parasitic elements to form a magneto-electric (ME) dipole array. Unlike conventional structures, this design incorporates a slot in the center of each rectangular patch. By optimizing the slot dimensions, the equivalent resonant frequency of the dipole can be flexibly tuned to match the target frequency band. This design further optimizes high-frequency impedance matching and enhances radiation performance at the upper edge of the operating band.

Through the synergistic optimization of the three-layer structure, the antenna element achieves highly efficient electromagnetic transmission. The overall dimensions are $7 \times 16.9 \times 3.048\,\text{mm}^3$. The planar model is shown in Fig. 2, and the detailed geometric parameters are listed in Table 1. This stacked configuration effectively achieves miniaturization while ensuring excellent electrical performance.

2.2. Power Splitter Design

For broadband array antennas, the bandwidth characteristics of the feeding network are just as critical as those of the antenna elements themselves. Series feeding networks typically exhibit narrow bandwidths due to their inherent phase-shift sensitivity and resonant characteristics, making them unsuitable for broadband designs. Therefore, this paper employs a corporate feeding topology based on SIW technology to design a 1-to-4 power divider with wideband characteristics.

To maintain consistency with the antenna elements in terms of materials and fabrication, the power divider is also implemented on a 1.016 mm thick Rogers 5880 dielectric substrate ($\varepsilon_r = 2.2$, $\tan\delta = 0.0009$). This power divider is constructed by cascading two stages of 1-to-2 SIW power dividers, as shown in Fig. 4. To improve impedance matching and suppress reflections, three metallized inductive vias (matching posts) are introduced at the T-junction of each stage. By optimizing the positions and dimensions of these vias to tune the local field distribution, reflection losses caused by structural discontinuities are effectively minimized.

In Fig. 3, the feeding slot on the bottom SIW is modeled as a parallel resonant circuit (L_{slot}, C_{slot}). Energy is transmitted through the SIW cavity and coupled to the subsequent layers via the magnetic current distribution of the slot. In the equivalent circuit, this coupling is represented by an ideal transformer (n : 1), with the turns ratio determined by the slot's dimensions and its offset relative to the SIW centerline. The middle-layer patch, serving as the primary radiator, is equivalent to a second resonant tank (L_d, C_d, R_{rad1}). Specifically, to characterize the physical properties of the wrench-shaped structure, an additional inductance L_{stub} is incorporated into this circuit. This inductance accounts for the inductive load introduced by the metallic extensions at the ends of the wrench-shaped structure. The introduction of L_{stub} effectively tunes the quality factor (Q) of this layer, thereby facilitating a broader resonant response. Finally, the top-layer parasitic patches are modeled as a third resonant circuit (L_p, C_p, R_{rad2}), which achieves near-field electromagnetic coupling with the middle layer through interlayer capacitance. This layer introduces an additional high-frequency resonance to enhance the bandwidth and gain at higher frequencies.

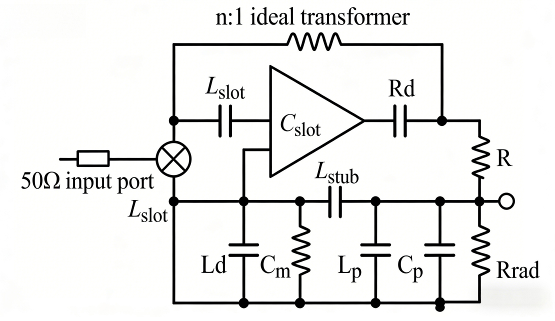

FIGURE 3. Equivalent circuit model.

Fig. 4 presents the simulated S-parameters of the designed power divider. It can be observed that within the target operating frequency range of 24.12 GHz to 30.83 GHz, the input return loss $|S_{11}|$ remains below -10 dB, satisfying the requirements for array feeding. Meanwhile, the transmission coefficients of the four output ports (S_{21}, S_{31}, S_{41}, and S_{51}) maintain excellent amplitude consistency across the entire band, indicating that the power divider achieves equal power distribution with low insertion loss. The simulation results verify that this power divider possesses superior transmission performance and stable power distribution over a wide bandwidth, meeting the feeding requirements of the proposed broadband array antenna.

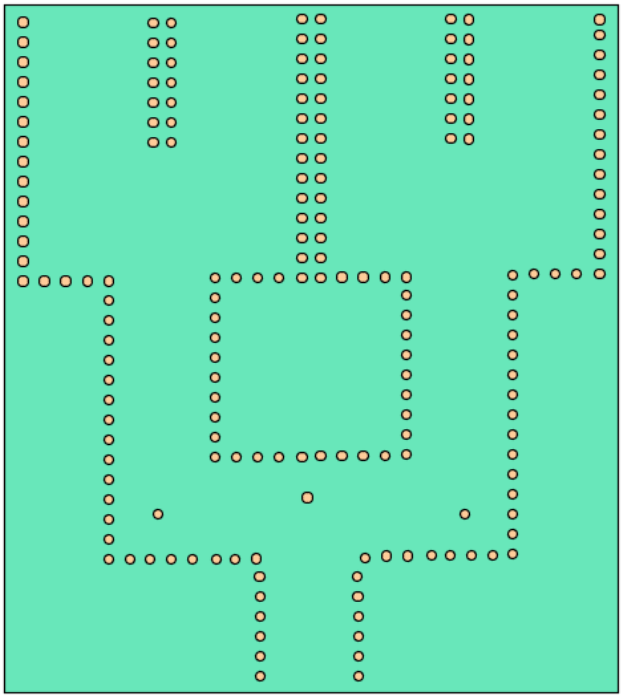

FIGURE 4. Planar structure diagram of power splitter.

Figure 5 displays the S-parameter simulation of the power divider. The S_{11} curve remains below-10dB across the target frequency band (24.12 GHz–30.83 GHz), meeting all design specifications. The S_{21}, S_{31}, S_{41}, and S_{51} curves converge closely, confirming the power divider's capability to distribute energy with equal amplitude and demonstrating excellent performance.

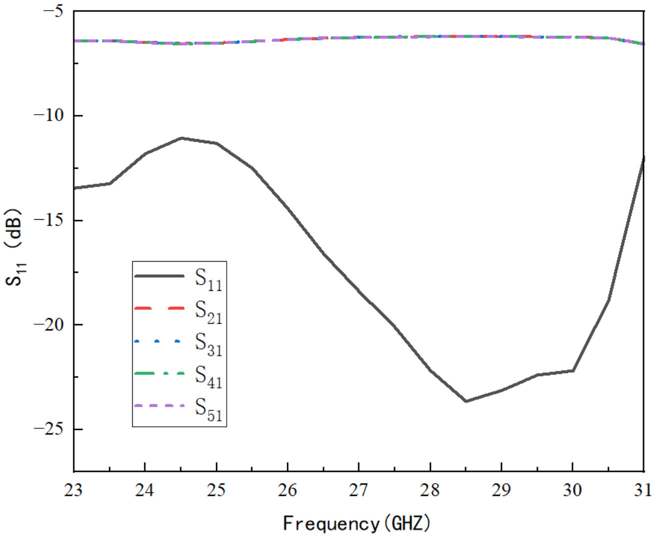

FIGURE 5. S-parameter diagram of power divider.

2.3. The Evolution of Antennas

Figure 6 illustrates the evolution of the antenna element's radiating patches. Focusing on the top-layer magnetic dipole's parasitic patches, the initial design (Antenna A) consists of traditional rectangular electric dipole elements. The integration of metallic vias introduces an additional resonance point and

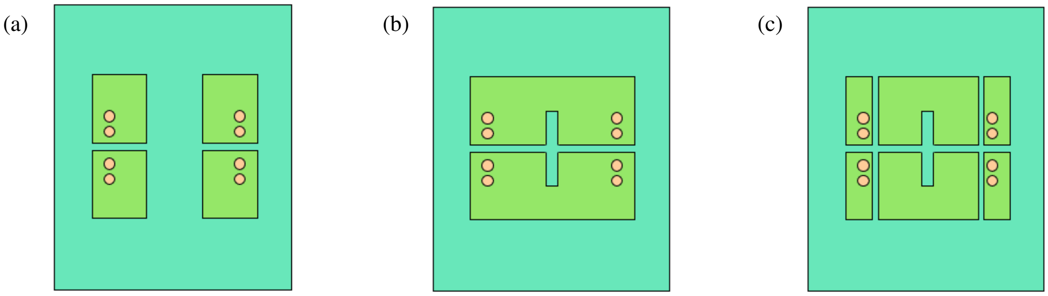

FIGURE 6. Diagram of the evolution of antennas.

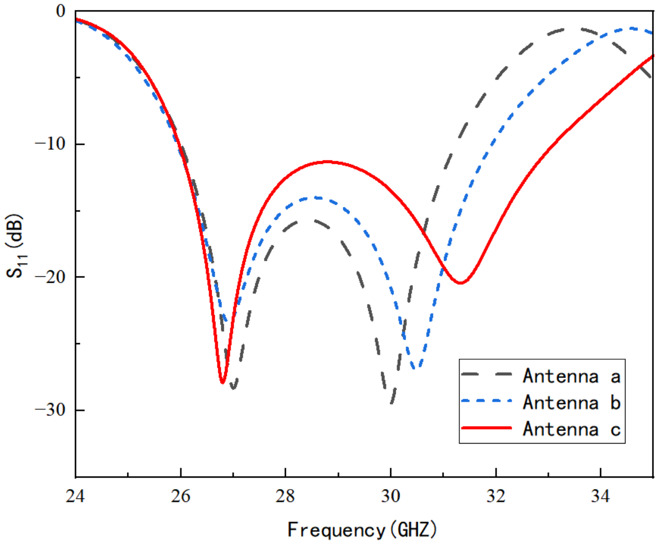

FIGURE 7. Comparison chart of antenna S-parameters.

directs a portion of the surface current to flow in the vertical direction, which effectively enhances electromagnetic coupling and achieves broadband performance. Antenna B merges the four rectangular patches of Antenna A into two pairs of upper and lower patches, incorporating rectangular gaps in the central region to achieve a more compact footprint. This modification strengthens the inter-patch coupling and facilitates efficient energy radiation across a wider frequency range. Finally, Antenna C involves splitting the two radiating patches of Antenna B into four sections. This configuration not only retains the broadband characteristics of the electric dipole but also forms a magnetic dipole through the central patches. The synergetic effect between the electric and magnetic dipoles further expands the bandwidth, while the optimized arrangement of the split patches enhances the overall radiation efficiency.

Figure 7 shows a comparison of the S-parameters for the three antennas. The initial four-patch dipole structure of Antenna A excites only two independent resonant modes. Although metallic vias are introduced for inductive compensation, the impedance matching between the two resonance peaks remains relatively weak. By merging the radiating elements and introducing a central slot, Antenna B maintains a stable low-frequency resonance while improving the matching depth in the 28–30 GHz range; meanwhile, the high-frequency resonance point shifts toward a higher frequency of approximately 30.5 GHz. Compared to the first two antenna structures, Antenna C not only preserves the dual-resonance characteristic facilitated by the inductive compensation of the metallic vias but also achieves a superior multi-mode superposition effect through the precise segmentation of the radiating patches. This structural modification enhances the electromagnetic coupling between the parasitic elements and the central radiator. Consequently, the resonant peaks of Antenna C exhibit a more uniform distribution and a flatter return loss profile; their mutual overlap leads to a significant expansion of the operational bandwidth.

2.4. Electric Field Analysis

In Fig. 8, at the first resonance frequency of 26.8 GHz, in (b) the second-layer patches function as an energy distribution network. The electric field is mainly distributed in the peripheral region of the patches, serving as the key parasitic structure for high-frequency mode control. In (a) the top-layer patches exhibit typical magnetoelectric (ME) dipole radiation characteristics. The electric field is highly concentrated around the central rectangular slit, forming a strong equivalent magnetic current. Energy is effectively coupled to the slot through the SIW cavity, exciting the magnetic dipole mode. Simultaneously, strong electric fields are distributed around the periphery of the four outer patches. At this frequency, the electric and magnetic dipoles achieve synchronous resonance, resulting in excellent impedance matching.

At the second resonance frequency of 31.34 GHz, in (d) the electric field of the second-layer radiating patch is significantly concentrated at its periphery. At this point, specific higher-order modes of the cavity are excited, and the parasitic elements on the top layer generate a secondary resonance due to the strong peripheral electric field in (c). This shift of the electric field distribution from the center to the periphery effectively introduces a new high-frequency resonance peak. By adjusting the outer dimensions and via positions of the second-layer patch, a smooth transition between this mode and the fundamental mode is achieved, thereby extending the impedance bandwidth beyond 33 GHz.

2.5. Array Antenna Design

By integrating the aforementioned antenna elements with a 1-to-4 corporate-feed power divider and optimizing the parame-

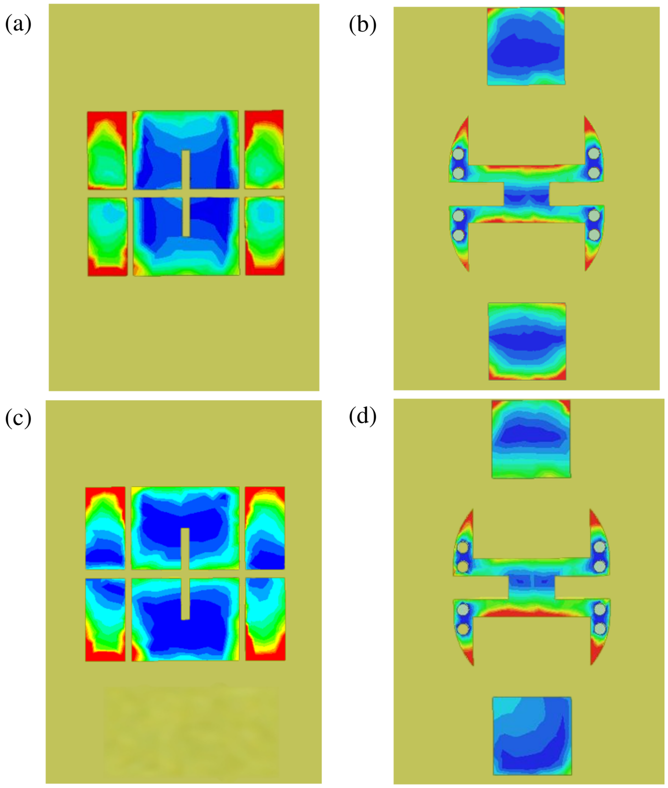

FIGURE 8. Electric field map of the patch at two resonance points.

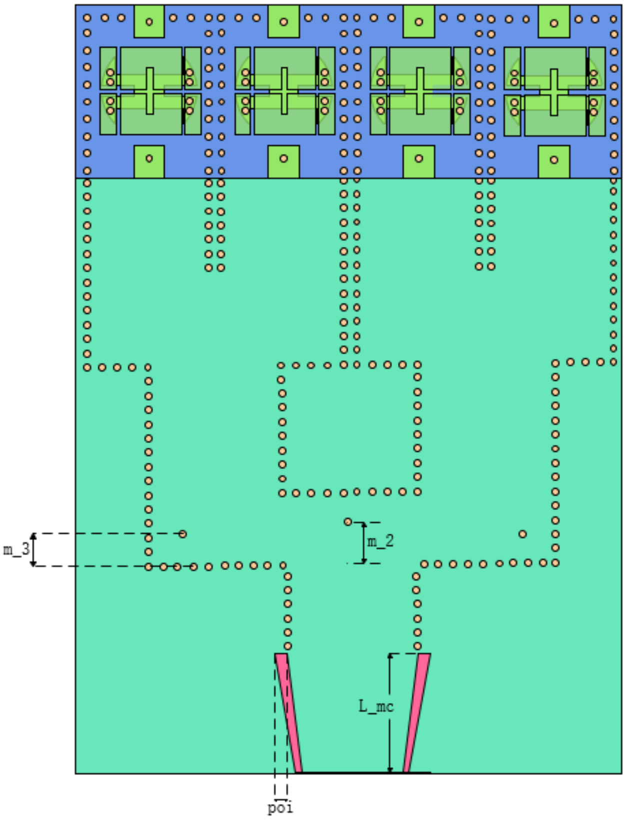

FIGURE 9. Schematic diagram of an antenna array.

ters, a 1 × 4 linear array was ultimately realized, as shown in Fig. 9.

The array utilizes a 1-to-4 equal-power divider based on a GCPW-to-SIW transition structure to feed the four magneto-electric (ME) dipole antenna elements. The overall dimensions of the antenna array are 26 mm × 49.6 mm × 3.048 mm, where each dielectric layer has a thickness of 1.016 mm and the copper cladding layer is 0.008 mm thick. To balance gain maximization and sidelobe suppression, the element spacing was optimized to $0.53\lambda_0$, where λ_0 is the free-space wavelength at the center frequency of 26.5 GHz.

The feeding interface of the array employs a grounded coplanar waveguide (GCPW) to SIW transition structure. The operating principle is that the tapered metal strip in the transition region guides the quasi-TEM mode field distribution of the GCPW to gradually transform into the TE_{10} mode of the SIW. This ensures good impedance matching and efficient energy transmission over a wide frequency band. Unlike conventional GCPW-to-SIW transitions, this design eliminates the metallized vias at the edges of the transition region and appropriately widens the signal line on the GCPW side. This modification offers two key advantages: first, it enhances the flexibility of impedance tuning at the GCPW port, facilitating better matching with the SIW; second, it reduces the ohmic losses introduced by excessive metal vias, thereby preventing a decline in radiation efficiency and maintaining stable gain characteristics across the operating band.

After integrating the elements with the power divider, the positions of the three metallized matching vias at each T-junction were fine-tuned to further optimize the overall impedance matching. The final geometric parameters of the antenna array are detailed in Table 2.

TABLE 2. Parameters and dimensions of the photovoltaic network.

parameter	size /mm	parameter	size /mm
m_2	3.25	L_mc	10
m_3	2.5	poi	1.2

3. SIMULATION TEST AND OPTIMIZATION ANALYSIS

Fig. 10 shows the E-plane and H-plane radiation patterns of the antenna unit, with a gain of 6.98 dBi per element. As shown in the figure, the half-power beamwidth (HPBW) of the main lobe is approximately 60°–80° in both the E-plane and H-plane, representing a moderate beamwidth that balances directivity and coverage. The rear lobe in the E-plane is slightly deeper than that in the H-plane, and the difference in current distribution across the two orthogonal planes is a typical characteristic of magnetic dipole radiation.

Fig. 11 displays the simulated $|S_{11}|$ results of the antenna array. The interconnected antenna elements exhibit a multiple resonance characteristic, achieving stable impedance matching

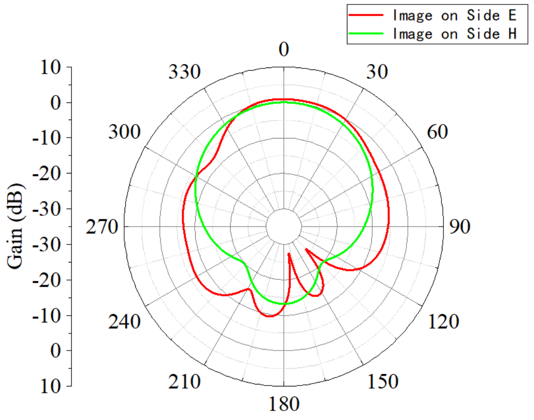

FIGURE 10. Antenna element pattern.

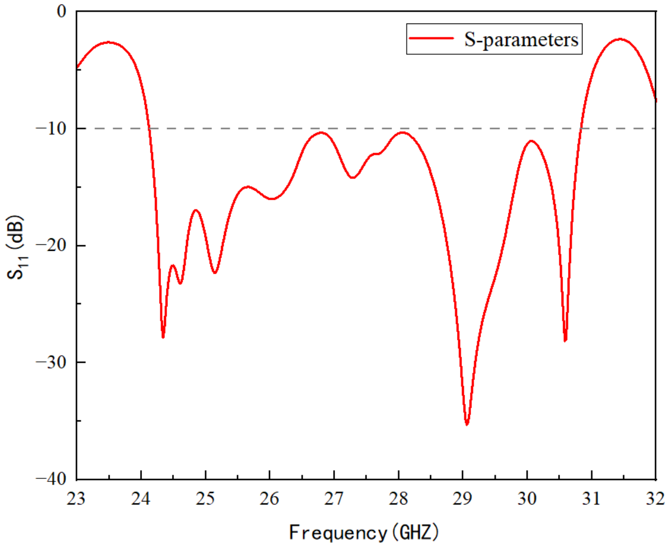

FIGURE 11. S-parameter simulation plots for array antennas.

below -10 dB within the 24.12 GHz–30.83 GHz range. This corresponds to a fractional bandwidth of 24.42%, which is slightly wider than that of a single element. Although the $|S_{11}|$ values show minor fluctuations within the band, they remain consistently below -10 dB, indicating that the mutual coupling between the elements is effectively controlled.

Fig. 12 presents the simulated radiation patterns of the antenna array. The 1×4 array achieves a peak gain of 11.02 dBi. The multi-lobed main beam, facilitated by the specialized feed transition structure, is optimized for wide-coverage communication. The sidelobes exhibit significantly lower power levels than the main lobe, demonstrating effective suppression of back radiation. Due to the excitation of higher-order modes within the stacked patch structure. As the frequency increases, the electrical size of the wrench-shaped patch and the parasitic elements becomes large enough to support non-radiating or destructive higher-order modes, leading to field cancellation in the broadside direction.

Due to impedance matching considerations, the dimensions of the feed transition structure significantly influence the radiation characteristics. Therefore, the parameters L_{mc} and poi have been optimized.

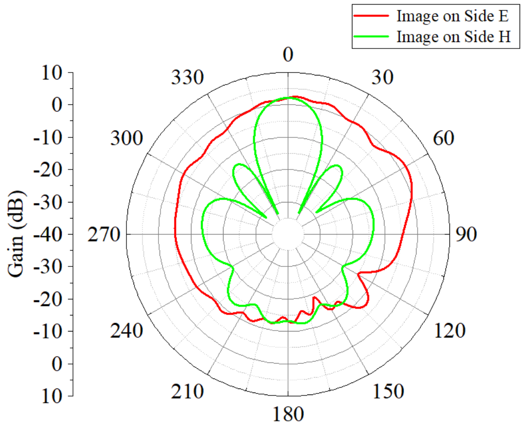

FIGURE 12. Antenna array diagram.

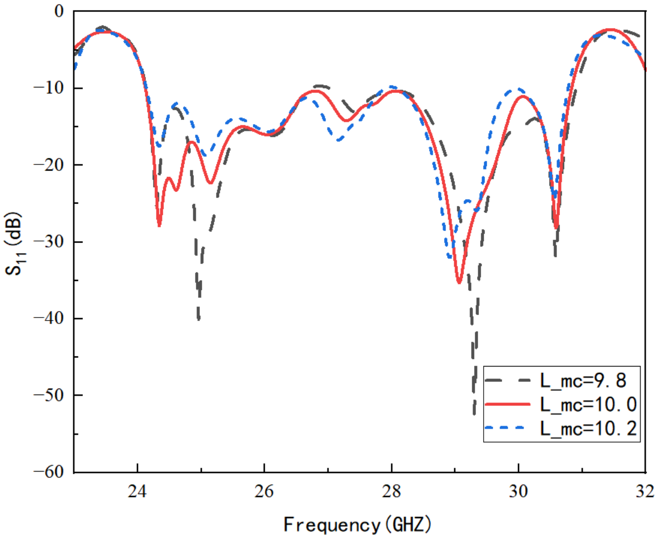

FIGURE 13. Effect of different L_mc values on S-parameters.

Fig. 13 displays the parametric sweep curves for the dual-gap spacing L_{mc}. This parameter directly determines the electromagnetic coupling strength between the two slots. When L_{mc} is set to 9.8 mm, the spacing is too narrow, leading to excessive near-field coupling that causes the input impedance to deviate from 50 Ω and degrades the $|S_{11}|$ performance. Conversely, at $L_{mc} = 10.2$ mm, the excessive spacing results in insufficient coupling and inadequate energy transfer, leading to increased insertion loss and reduced bandwidth. Consequently, the optimal spacing L_{mc} is determined to be 10 mm.

Figure 14 illustrates the influence of the characteristic length R, at the terminals of the second-layer wrench-shaped patch, on the antenna's S-parameters. The parameter R primarily determines the equivalent electrical current path of the middle-layer radiator and, consequently, the resonant frequency it excites. As R decreases (e.g., to 1.8 mm), an impedance mismatch occurs between 26 GHz and 29 GHz because the multi-mode superposition effect is insufficiently developed, leading to a narrower operational bandwidth. Conversely, as R increases (e.g., to 2.2 mm), a slight mismatch appears near 26 GHz, and the

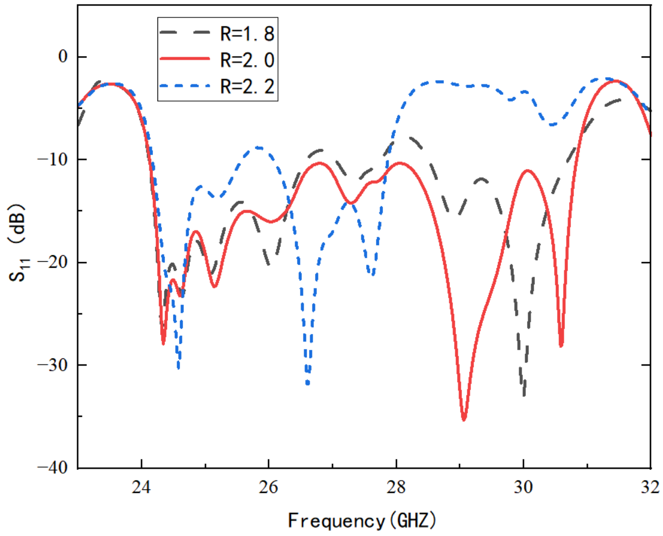

FIGURE 14. The effect of different R sizes on S-parameters.

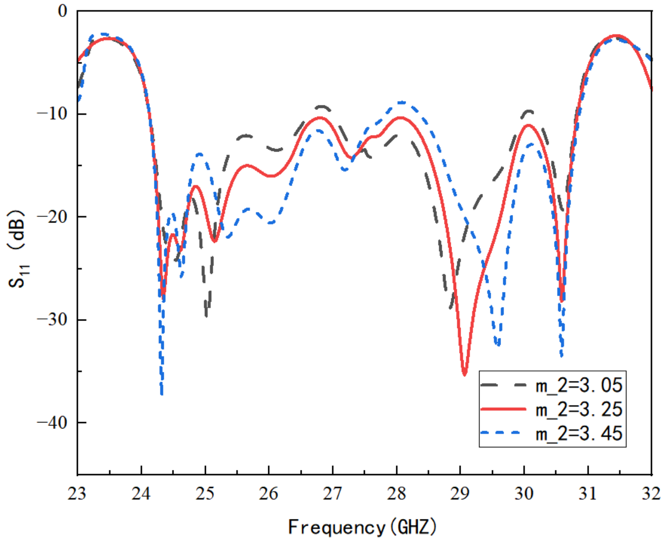

FIGURE 15. Effect of different m_c values on S-parameters.

high-frequency resonance points shift significantly toward the lower frequencies. In this case, certain modes fail to merge effectively, resulting in reduced resonance depth. When R is optimized at 2.0 mm, the return loss performance is maximized, ensuring that the energy exchange between the bottom-layer slot, the middle-layer driver, and the top-layer parasitic elements reaches a critical coupling state. This configuration enables the antenna to excite multiple resonant modes while maintaining a low-profile characteristic.

By introducing three metallized matching vias at the T-junctions of each stage in the power divider and optimizing their relative positions and spacing, the local equivalent impedance at the junction points can be effectively adjusted. This suppresses the excitation of higher-order modes, reduces energy reflection and transmission losses, and improves the reflection coefficient $|S_{11}|$ at the input port. Among these, the distance m_2 between the center via and the bottom metal wall is a key parameter affecting impedance matching.

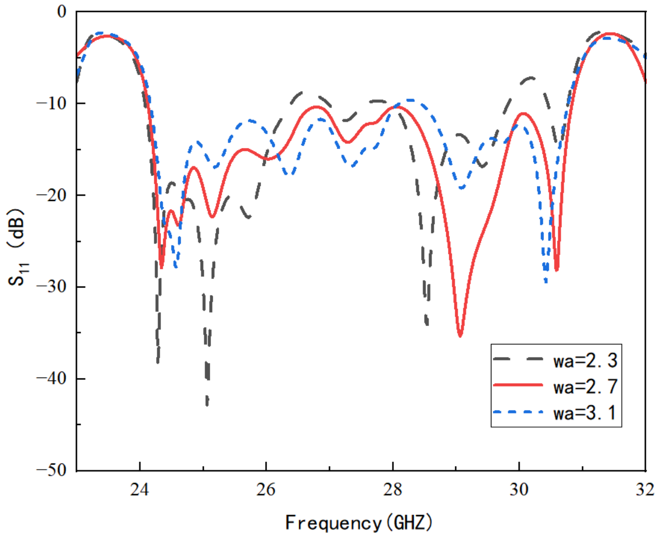

FIGURE 16. Effect of different wa values on S-parameters.

Fig. 15 illustrates the simulated $|S_{11}|$ curves for different m_2 values. It is evident that m_2 significantly impacts the impedance matching across the entire operating frequency band. When m_2 decreases, the antenna exhibits significant mismatch across most of the band, and the $|S_{11}|$ curve shifts upward (deteriorates) overall, with some frequency points exceeding the -10 dB threshold. Conversely, as m_2 increases, although matching improves in certain sub-bands, regions of impedance mismatch persist, and the in-band flatness remains poor, which is detrimental to stable broadband operation. A comprehensive comparison of the matching performance indicates that when $m\_2 = 3.45$ mm, the antenna maintains optimal impedance matching throughout the target frequency band, with $|S_{11}|$ remaining consistently below -10 dB and exhibiting minimal fluctuations. Therefore, the optimal distance between the center matching via and the bottom wall is determined to be 3.45 mm.

As illustrated in Fig. 16, variations in the width of the top-layer parasitic patch (w_a) have a significant impact on the array's return loss. When $w_a = 2.3$ mm, the relatively small electrical dimension of the parasitic element causes its resonant frequency to shift upward, leading to weak coupling with the middle-layer driven mode. This results in an unsatisfactory return loss (approaching -10 dB) in both the mid- and high-frequency bands, leaving an insufficient bandwidth margin. Conversely, when w_a is increased to 3.1 mm, the resonant frequency shifts significantly toward the lower frequencies due to the excessive equivalent electrical length of the parasitic patch. This causes the previously merged modes to decouple, resulting in an impedance mismatch near 28 GHz. When w_a is optimized at 2.7 mm, a robust resonance is excited near 30.5 GHz. In this configuration, the parasitic mode perfectly overlaps with the resonant mode of the middle-layer wrench-shaped patch, achieving an optimal matching depth and a flat response across the entire operating bandwidth.

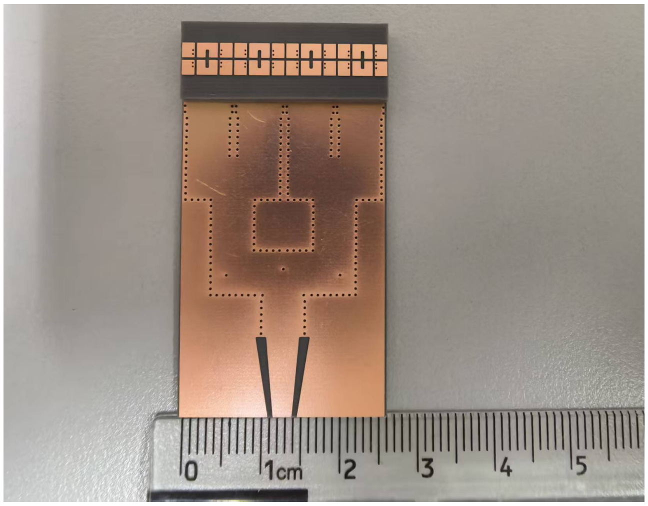

FIGURE 17. Antenna physical image.

4. MEASUREMENT AND ERROR ANALYSIS

As shown in Table 3, a comparison of the proposed antenna array with the SIW-fed antennas reported in [19–22] reveals the following. The design in [19] employs an SIC cavity and a crescent-shaped parasitic patch structure to achieve an effective bandwidth of 21.3% and a gain of 14.5 dBi in the Ku band. Ref. [20] uses a three-layer SIW feed network and a four-layer laminated structure to obtain a bandwidth of 19.35% and a gain of 17.1 dBi in the Ku band. Ref. [21] incorporates a magneto-dipole and L-shaped parasitic patches to achieve an impedance bandwidth of 21.8% and a gain of 14.1 dBi in the millimeter-wave band. Furthermore, Ref. [22] utilizes a two-layer SIW feed network and an air cavity structure to realize a bandwidth of 16.3% and a high gain of 26.7 dBi in the 5G millimeter-wave band.

TABLE 3. Comparison of antenna performance.

Ref.	Freq.band (GHz)	Array size	FBW (%)
[19]	10.74–13.30	2 × 2	21.3
[20]	11.2–13.6	4 × 4	19.35
[21]	29.28–35.83	2 × 2	21.8
[22]	35.4–41.7	8 × 8	16.3
Work	24.12–30.83	1 × 4	24.42

In contrast, the proposed antenna features a miniaturized 1 × 4 array, covering the 24.12–30.83 GHz frequency band, which fully encompasses the mainstream 5G millimeter-wave bands in China, Europe, and the United States. Its relative bandwidth reaches 24.42%, outperforming the designs in the aforementioned literature. Although its peak gain of 11.02 dBi is lower than that of larger-scale arrays, the proposed antenna achieves a favorable balance between broadband performance and stable radiation characteristics within a compact footprint of 26 mm × 49.6 mm.048 mm. This fully demonstrates its comprehensive performance advantages for millimeter-wave broadband applications.

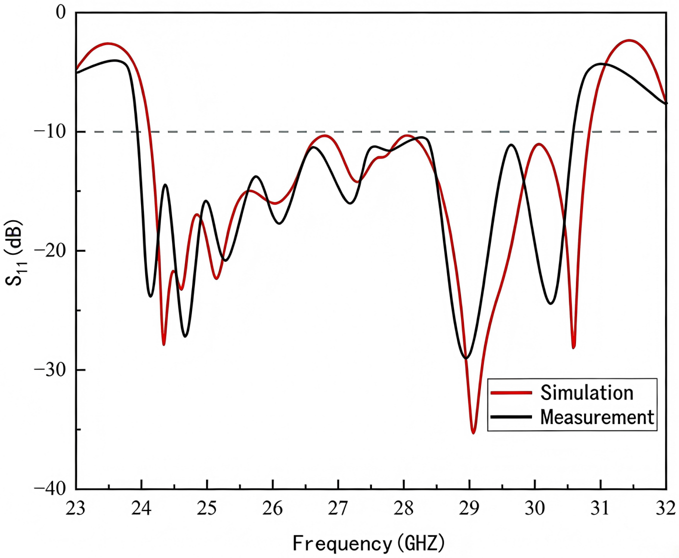

FIGURE 18. Comparison between simulated and measured results.

Fig. 17 shows a photograph of the fabricated antenna array. During the manufacturing process, to minimize performance deviations caused by assembly misalignments, the three-layer dielectric substrate was integrated using a lamination bonding process rather than the conventional method of manual alignment with auxiliary holes. This approach effectively reduced additional losses and fabrication tolerances, resulting in measured performance that closely aligns with the simulation results. As illustrated in the figure, the antenna array exhibits a compact footprint and a highly integrated structure, successfully achieving the objectives of miniaturization and cost-effectiveness.

The comparison between the S-parameters of the antenna's actual test and simulation results is shown in Fig. 18. The simulation results indicate that there is a certain discrepancy between the measured and simulated curves. While the actual test curve generally follows the simulation trend, it shows a slight shift toward lower frequencies than the simulation, with the overall deviation being less than 5%. This discrepancy is primarily caused by manufacturing process errors and measurement system inaccuracies. Although the three-layer antenna employs lamination technology to avoid losses from drilling, factors such as interlayer alignment deviations, dielectric thickness variations, dielectric constant drift, and metallization via hole errors during the multi-layer lamination process can disrupt structural symmetry and impedance continuity. These factors lead to resonant frequency shifts and changes in coupling strength, affecting the matching performance at certain frequency points during testing. Additionally, residual calibration errors from the vector network analyzer, variations in probe contact impedance, test cable losses, and environmental electromagnetic interference can introduce extra fluctuations in the measured curves. Although the combined errors result in slightly inferior performance compared to simulations, the overall trend remains consistent, demonstrating the antenna structure's sound rationality.

5. SUMMARY

This paper proposes a three-layer 1×4 dipole broadband antenna array based on a substrate-integrated waveguide (SIW) with slot-coupled feeding. The antenna adopts a stacked configuration to achieve a compact structure. Rectangular coupling slots are etched in the SIW cavity of the bottom layer to enable efficient longitudinal energy coupling from the feeding layer to the upper layers.

The middle layer incorporates a wrench-shaped patch, which broadens the impedance bandwidth by forming a dual-resonant circuit. In addition, symmetrically loaded rectangular patches on both sides help maintain radiation pattern stability across the entire operating frequency band. The top layer employs a slotted dipole parasitic patch structure to further improve impedance matching and expand the operating bandwidth.

Both simulation and measurement results demonstrate that the proposed antenna array operates from 24.12 GHz to 30.83 GHz, corresponding to a relative bandwidth of 24.42%. The in-band gain remains stable, with a maximum value of 11.02 dBi. While extending the bandwidth, the proposed design effectively suppresses higher-order mode propagation and stray current distribution, thereby improving radiation purity. Owing to its compact structure, low cost, and miniaturization capability, the proposed antenna shows promising potential for millimeter-wave wireless communication systems.

Compared to cavity-backed or conventional stacked patch antennas, which have been extensively investigated in existing literature, the unique contribution of this work lies in the precise control of multi-modal resonances through a custom-designed "wrench-shaped" radiator. Traditional schemes often suffer from degraded in-band matching due to insufficient mode merging. In contrast, the structure proposed in this paper incorporates inductive branches into the main radiating element, effectively modulating the resonator's quality factor and facilitating an ideal critical coupling state among the bottom-layer slot, the middle-layer driven patch, and the top-layer parasitic elements. This approach not only achieves an ultra-wide fractional impedance bandwidth of 24.42% but also significantly enhances the array's radiation efficiency and gain flatness without necessitating additional decoupling structures. Consequently, it provides a highly integrated, high-performance solution for millimeter-wave 5G systems.

ACKNOWLEDGEMENT

This work was supported by the Applied Basic Research of Liaoning Province (2022JH2/101300275) and the University-local government scientific and technical cooperation cultivation project of Ordos Institute-LNTU (YJY-XD-2024-B-009)

REFERENCES

[1] Cheng, Y. J., *Substrate Integrated Antennas and Arrays*, CRC Press, 2018.

[2] Chen, Z. N. and X. Qing, *Substrate-Integrated Millimeter-Wave Antennas for Next-Generation Communication and Radar Systems*, John Wiley & Sons, 2021.

[3] Chandelkar, A., A. Kumar, P. Jadhav, A. A. Althuwayb, and K. Aliqab, "Semi circular SIW cavity coupled patch filtenna," *IEEE Access*, Vol. 13, 37 865–37 871, 2025.

[4] Hong, W., K. Wu, H. Tang, J. Chen, P. Chen, Y. Cheng, and J. Xu, "SIW-like guided wave structures and applications," *IEICE Transactions on Electronics*, Vol. 92, No. 9, 1111–1123, 2009.

[5] Cui, L., J. Li, H. Wu, Y. Bai, and X. Zheng, "Design of ka-band millimeter-wave slot antenna based on substrate-integrated waveguide," *Journal of Microwaves*, Vol. 40, No. 3, 12–16, 2024.

[6] Xu, F. and K. Wu, "Guided-wave and leakage characteristics of substrate integrated waveguide," *IEEE Transactions on Microwave Theory and Techniques*, Vol. 53, No. 1, 66–73, 2005.

[7] PourMohammadi, P., H. Naseri, N. Melouki, F. Ahmed, A. Iqbal, G. A. E. Vandenbosch, and T. A. Denidni, "Compact SIW-based self-quadruplexing antenna for microwave and mm-Wave communications," *IEEE Transactions on Circuits and Systems II: Express Briefs*, Vol. 70, No. 9, 3368–3372, 2023.

[8] Naseri, H., P. PourMohammadi, A. Iqbal, A. A. Kishk, and T. A. Denidni, "SIW-based self-quadruplexing antenna for microwave and mm-Wave frequencies," *IEEE Antennas and Wireless Propagation Letters*, Vol. 21, No. 7, 1482–1486, 2022.

[9] Wang, Q. and J. Liu, "Design of miniaturized broadband microstrip antennas based on artificial electromagnetic structures," *Journal of Microwave Science*, No. S1, 38–42, 2017.

[10] Ghassemi, N., K. Wu, S. Claude, X. Zhang, and J. Bornemann, "Low-cost and high-efficient W-band substrate integrated waveguide antenna array made of printed circuit board process," *IEEE Transactions on Antennas and Propagation*, Vol. 60, No. 3, 1648–1653, 2012.

[11] Ghassemi, N. and K. Wu, "High-efficient patch antenna array for E-band gigabyte point-to-point wireless services," *IEEE Antennas and Wireless Propagation Letters*, Vol. 11, 1261–1264, 2012.

[12] Cheng, Y. J., Y. X. Guo, and Z. G. Liu, "W-band large-scale high-gain planar integrated antenna array," *IEEE Transactions on Antennas and Propagation*, Vol. 62, No. 6, 3370–3373, 2014.

[13] Luo, G. Q., Z. F. Hu, L. X. Dong, and L. L. Sun, "Planar slot antenna backed by substrate integrated waveguide cavity," *IEEE Antennas and Wireless Propagation Letters*, Vol. 7, 236–239, 2008.

[14] Luo, G. Q., Z. F. Hu, W. J. Li, X. H. Zhang, L. L. Sun, and J. F. Zheng, "Bandwidth-enhanced low-profile cavity-backed slot antenna by using hybrid SIW cavity modes," *IEEE Transactions on Antennas and Propagation*, Vol. 60, No. 4, 1698–1704, 2012.

[15] Xu, J., W. Hong, Z. H. Jiang, and H. Zhang, "Wideband, low-profile patch array antenna with corporate stacked microstrip and substrate integrated waveguide feeding structure," *IEEE Transactions on Antennas and Propagation*, Vol. 67, No. 2, 1368–1373, 2019.

[16] Tong, X., Z. H. Jiang, C. Yu, F. Wu, X. Xu, and W. Hong, "Low-profile, broadband, dual-linearly polarized, and wide-angle millimeter-wave antenna arrays for Ka-band 5G applications," *IEEE Antennas and Wireless Propagation Letters*, Vol. 20, No. 10, 2038–2042, 2021.

[17] Park, S.-J., D.-H. Shin, and S.-O. Park, "Low side-lobe substrate-integrated-waveguide antenna array using broadband unequal feeding network for millimeter-wave handset device," *IEEE Transactions on Antennas and Propagation*, Vol. 64, No. 3, 923–932, 2016.

[18] Pramodini, B., D. Chaturvedi, L. Darasi, G. Rana, and A. Kumar, "Optimized compact MIMO antenna design: HMSIW-based and

cavity-backed for enhanced bandwidth," *IEEE Access*, Vol. 12, 189 820–189 828, 2024.

[19] Wang, X.-C., J.-H. Yang, Z.-G. Yan, Y.-J. Xia, and W.-Z. Lyu, "Ku-band broadband high-gain substrate integrated cavity circularly polarized antenna array," *Journal of Microwaves*, Vol. 38, No. 3, 8–13, 2022.

[20] Karami, F., P. Rezaei, A. Amn-e Elahi, A. Abolfathi, and A. A. Kishk, "Broadband and efficient patch array antenna fed by substrate integrated waveguide feed network for Ku-band satellite applications," *International Journal of RF and Microwave Computer-Aided Engineering*, Vol. 31, No. 9, e22772, 2021.

[21] Xu, J., Y. Xie, and J. Zhao, "SIW broadband circularly polarized high-gain low-profile magneto-electric dipole antenna array," *Microwave and Optical Technology Letters*, Vol. 66, No. 11, e70033, 2024.

[22] Li, X., J. Xiao, Z. Qi, and H. Zhu, "Broadband and high-gain SIW-fed antenna array for 5G applications," *IEEE Access*, Vol. 6, 56 282–56 289, 2018.

[23] Wang, J., Y. Li, J. Wang, L. Ge, M. Chen, Z. Zhang, and Z. Li, "A low-profile vertically polarized magneto-electric monopole antenna with a 60% bandwidth for millimeter-wave applications," *IEEE Transactions on Antennas and Propagation*, Vol. 69, No. 1, 3–13, 2021.